J Solid State Electrochem (2008) 12:545–552
DOI 10.1007/s10008-007-0331-3

ORIGINAL PAPER

Corrosion crack enhancement during the cathodic activation of zirconium AB_2 alloys

J. O. Zerbino · A. Visintin · W. E. Triaca

Received: 20 June 2006 / Revised: 5 August 2006 / Accepted: 5 August 2006 / Published online: 23 May 2007

Abstract The activation of zirconium nickel alloys with and without the addition of chromium and titanium is investigated through electrochemical and optical techniques. Recent investigations in aqueous 1 M KOH indicate oxide layer growth and occlusion of hydrogen species in the alloys during the application of different cathodic scan potential programmes currently used for the activation process. In this research, several techniques, such as voltammetry, ellipsometry, energy dispersive analysis of X-rays and scanning electron microscopy, are applied to three polished massive alloys, $Zr_{1-x}Ni_x$, x=0.36 and 0.43, and $Zr_{0.9}Ti_{0.1}NiCr$. Data analysis shows that the stability, compactness and structure of the passive layers are strongly dependent on the applied potential programme. The alloy activation depends on the formation of deep crevices that remain after further polishing. The microscopic observation shows an increase in crevice thickness after cathodic sweep potential cycling, which produces fragmentation of the grains and oxide growth during the activation process. This indicates metal breaking and intergranular alloy dissolution that take place together with oxide and hydride formation. In some cases, the resultant crevice thickness is one or two orders higher than the growth of surface oxide indicating localised intergranular corrosion.

Dedicated to Prof. Dr. Teresa Iwasita on the occasion of her 65th birthday in recognition of her numerous contributions to interfacial electrochemistry.

J. O. Zerbino (✉) · A. Visintin · W. E. Triaca
Instituto de Investigaciones Fisicoquímicas Teóricas y Aplicadas,
INIFTA. UNLP. Comisión de Investigaciones Científicas,
CIC. CONICET.,
C.C. 16 Suc. 4.,
1900 La Plata, Argentina
e-mail: jzerbino@inifta.unlp.edu.ar

Keywords Hydrogen absorption · Zirconium and nickel oxides · Metal hydride · Rechargeable batteries · Ellipsometry · Composite materials

Introduction

With the development of fuel cell technology and the widening of hydrogen application processes, hydrogen storage has attracted increasing attention. The new alloys developed to have higher hydrogen storage capacity and lower plateau pressure may be divided into AB_2 and AB_5 types. Ti and Zr correspond to the element A side of the AB_2 type alloy. These alloys have the structure of Laves phase [1–5]. Although they do not show any activation difficulty during hydrogen absorption from the gas phase, they exhibit a slow activation rate in the electrolyte [6–8]. Some mechanisms exclude the existence of thin semiconductive oxide films, which are certainly spontaneously formed on the alloy surface in aqueous electrolytes [3, 5, 9, 10]. Of a great interest is how and when the oxide layer is reduced, accompanied by hydrogen and hydride formation [1–13].

These alloys are activated by potential cycling in the cathodic region. Recent work shows that, although at cathodic potentials, the incipient oxide is protonated rather than eliminated; it continues to grow in thickness [1, 12–15]. Several studies on hydrogen behaviour in ZrO_2 oxide have been carried out. However, literature data for hydrogen solubility and diffusivity show some uncertainty and discrepancies [16, 17]. The structure of these oxide layers is strongly dependent on the electrolyte composition, the potential and the history applied to the samples [18, 19]. Previous work shows that anodically formed oxide on Ti–50%Zr alloy has a rate growth twice higher than that observed on Zr [20]. Moreover, potential cycling treatments

of a Ti electrode in the cathodic region produce the protonation of the oxide, depassivating the oxide layer and partly reducing Ti^{+4} to Ti^{+3}. Ti^{+3} defects promote water dissociative adsorption onto TiO_2 surfaces and are linked to surface porosity [21].

On the other hand, the particular quality arising from the small cross-section of Zr and Zr alloys for neutron absorption makes them suitable as covering material for nuclear fuels. However, the combination of radiation, oxidation and hydriding degrades the behaviour of fuel cladding during nuclear reactor operation [14, 22], and the determination of the operating mechanism is a very complex and difficult aspect in the stress corrosion cracking observed [23–26]. Furthermore, the great demand for stable lightweight and biocompatible materials makes the corrosion and passivation of these alloys worthy of intensive studies [20].

The purpose of the present work is to analyse the surface structure changes of ZrNi and ZrTCrNi alloys produced during activation by voltammetry, ellipsometry, scanning electron microscopy (SEM) and energy dispersive analysis of X-rays (EDAX). The evolution of the interface and the limit grain structure are correlated with changes in hydrogen storage capacity.

Experimental

The optical cell was similar to that previously reported [1, 12]. All electrochemical experiments were performed using a reversible hydrogen electrode in the same solution as that of the reference electrode. The alloys, $Zr_{1-x}Ni_x$, x=0.36 and 0.43 and $Zr_{0.9}Ti_{0.1}NiCr$ were prepared by melting the elements in a water cooler crucible and were turned over and remelted to ensure homogeneity [1, 3]. The alloy pellet was mounted on a Teflon holder, sheathed in Araldite resin and mechanically polished with fine grade emery paper and different powder alumina of 1, 0.3 and 0.05 μm. The 1 M KOH solution was prepared from a.r Merck p.a. and thrice distilled water. The Pt counter electrode, located in a separated compartment, was connected through a fretted glass plaque. Runs were made at 25 °C under purified N_2 gas bubbling.

The ellipsometric measurements were made in a Rudolph Research type 437-02/200 B manual ellipsometer provided with a 150 W tungsten lamp and an RCA 1P21 photomultiplier. Data were obtained at λ=546 nm and λ= 450 nm with an incident and reflected angle of 70°. The tested optical area of about 2 mm^2 was centred on the larger grain. The ellipsometric parameter Δ indicates the phase shift of the electric vectors (*Es*, *Ep*) and tangent Ψ the change in amplitude ratio of these components after light beam reflection. It should be remarked that these ellipsometric measurements operating in the null mode are independent of intensity variations produced by eventual isolated crevice development on the surface.

The refractive indices and thickness of the oxide were calculated assuming a single homogeneous film. The programme employed for the calculation uses the subroutine IBM-DFMCG to find the local minimum of a complex function of several variables by the method of conjugated gradients [1]. The fitting procedure minimises the function G

$$G=\sum\left(\Delta_{ij}^{\mathrm{ex}}-\Delta_{ij}^{\mathrm{the}}\right)^2+\left(\Psi_{ij}^{\mathrm{ex}}-\Psi_{ij}^{\mathrm{the}}\right)^2$$

where the subindex i corresponds to the experimental optical data, Δ^{ex}, Ψ^{ex}, measured at different λ_i, and the subindex j to different cycling times or thickness, d_j. After m iteration, the optimisation method converges to theoretical values $\Delta_{ij}^{\mathrm{the}}$ and Ψ_{ij}^{the}. The convergence is filled for increasing m when: (a) the euclidean norm of the arrangement, p_m-p_{m+1}, tends to 0, (b) $G(p_m)>G(p_{m+1})>G(p_{m+2})$ and (c) $\partial G_m/\partial p$ tends to 0.

The phase morphology of the intermetallic sample was also analysed through SEM micrographs collected by a Philips (XL30) microscope operating at 20 kV, which was coupled with an energy dispersive chemical analysis microprobe (EDAX). Before activation, the surface analysis was made first on the polished samples, without any additional re-cover metallic treatment. After activation, the electrode surface was polished for only 4 min with 0.05-μm alumina eliminating the more external oxide layer with the specific aim of improving the optical contrast of the granular structure.

Results and discussion

Voltammetric data

Figure 1 shows the voltammetric (i/E) response of three alloys, namely, ($Zr_{0.36}Ni_{0.64}$), ($Zr_{0.43}Ni_{0.57}$) and ($Zr_{0.9}Ti_{0.1}$ NiCr), which are, henceforth, named Zn_1, Zn_2 and B_6. The potential cycle starts by cathodically scanning from the open circuit potential *Eoc* down to the cathodic limit *Ec*, followed by anodic scanning up to the anodic limit *Ea*. The first i/E cycles for the fresh non-activated Zn_1 surface are displayed in Fig. 1a, while the i/E response for the same alloy, but after cycling for 3 h and a further new complete polishing, is shown in Fig. 1b. The cathodic current at potentials E<0 V indicates hydrogen evolution, and a progressive increase in cathodic current is also observed by increasing the number of cycles. Figure 1b shows a significant increase in anodic currents after prolonged cycling, which indicates oxidation of occluded hydrogen.

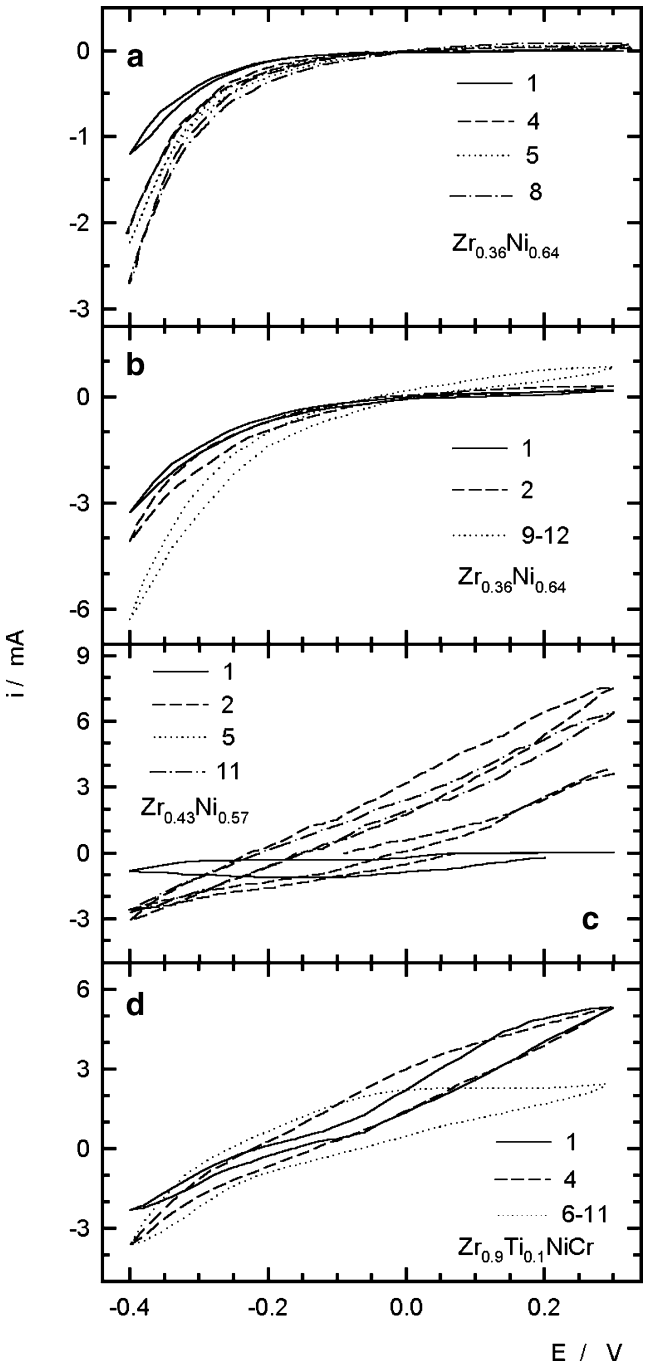

Fig. 1 Potential scan starting at E_{oc}=0.25 V to the cathodic limit E_c=−0.4 V and then cycling to E_a=0.3 V; **a** and **b** $Zr_{0.36}Ni_{0.64}$, **c** $Zr_{0.43}Ni_{0.57}$ and **d** $Zr_{0.9}Ti_{0.1}NiCr$. The *figures* indicate the number of cycles

The *i*/*E* response of the Zn_2 and B_6 alloys during cycling looks similar to the former (Fig. 1c,d). However, the progressive increase in both the cathodic and anodic currents is remarkably more effective than that shown in Fig. 1a. Moreover, in the B_6 case, there is a further decrease in anodic current for increasing cycling time (Fig. 1d).

The anodic current indicates contributions of growth of the passivated oxide layer and the oxidation of occluded hydrogen in the oxide/metal interface. The hydrogen evolution rate gradually increases with the successive cycles. This effect indicates an increase in concentration of absorbed hydrogen that progressively accumulates in the metal/oxide interface promoting the gaseous hydrogen discharge [1, 27]. The small hysteresis caused by the autocatalytic hydrogen evolution is similar to that already observed on passive Hf [14].

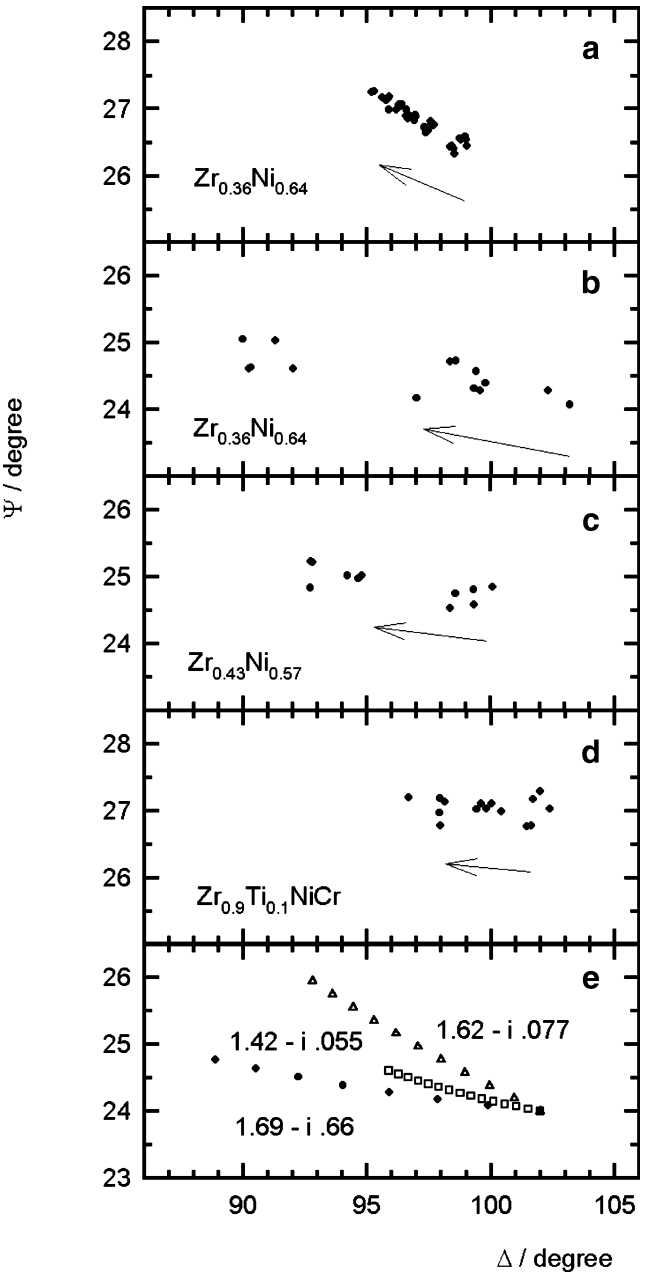

Fig. 2 Change in the ellipsometric parameters Δ and Ψ during cycling between E_c=−0.4 V and E_a=0.3 V; **a** and **b** $Zr_{0.36}Ni_{0.64}$, **c** $Zr_{0.43}Ni_{0.57}$ and **d** $Zr_{0.9}Ti_{0.1}NiCr$; **e** theoretical curves for optical indices: n=1.62−i 0.077, 1.69−i 0.66, 1.42−i 0.55 and increasing thickness every 1 nm

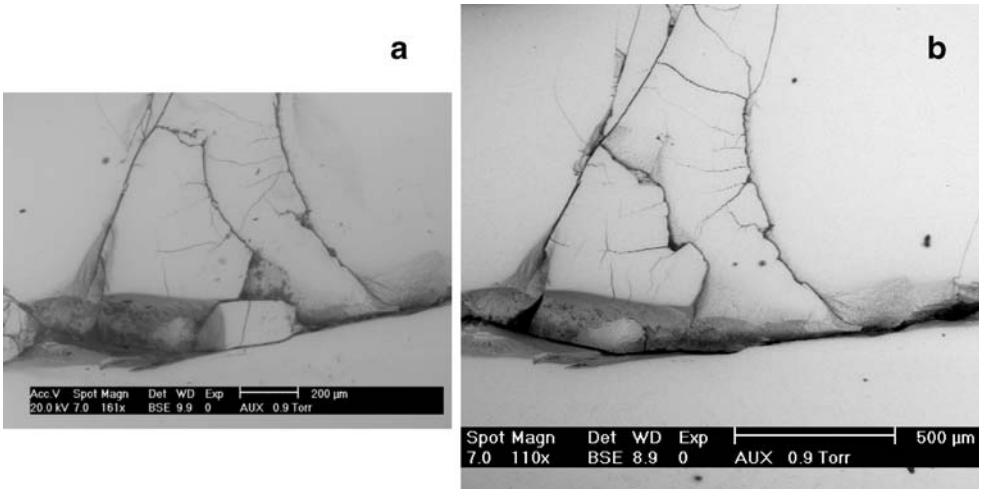

Fig. 3 Image of the $Zr_{0.36}Ni_{0.64}$ alloy before (**a**) and after (**b**) potential cycling in 0.1 M KOH

Ellipsometric data

The change of the optical parameters Δ and Ψ for Zn_1, Zn_2 and B_6 alloys during potential cycling between −0.4 and 0.3 V is shown in Fig. 2a–d. The point with higher Δ value, Δ_o, corresponds to the recently polished surface at open circuit potential, E_{oc}. The Ψ change linearly follows the Δ variation. In these experiments, the Δ decrease is directly linked with d, the increase in oxide layer thickness [1]. Figure 2e shows theoretical Δ and Ψ values resulting from fitting the experimental data assuming a single homogeneous and isotropic layer and increments in the oxide layer thickness, d, every 1 nm.

In these calculations, thickness d_o, the thin passive layer spontaneously formed at open circuit potential, is neglected, and the calculated d corresponds to the thickness increase during cycling, that is $d=d_{\text{oxide}}-d_o$ [1]. The d_o value found on Zr and on these alloys is relatively small and is estimated as about 5 nm [1, 14, 28]. The precise evaluation of both d_o and the optical indices corresponding to the substrate in the different alloys is beyond the scope of this work. The variation in the initial Δ_o and Ψ_o values obtained for the different polished alloys depends on: (1) window effects of the optical cell emplacement, (2) variation of the optical constant for the different substrates and (3) differences in thickness of the thin passive layer spontaneously formed at open circuit d_o. The fitted calculated thickness, d, and the optical indices of the oxide layer, $n-i\,k$, are independent of the observed small Δ_o/Ψ_o shift, in agreement with data reported in previous work [1, 29].

In Fig. 2a, the potential cycling is applied to the recently prepared Zn_1 alloy, before any activation treatment. On the other hand, Fig. 2b shows the optical response of the same alloy substrate but after bearing 5 h of activation treatment and further mechanical polishing using alumina 1, 0.3 and 0.05 µm during successive time periods of 10, 5 and 5 min, respectively. The very different optical response indicates changes in the substrate. Moreover, after activation, polishing does not restore the surface initial state. The optical index values $n-i\,k$ obtained by fitting are equal to 1.62−i 0.077 and 1.69−i 0.66, and a total thickness variation, d, of 6 and 8 nm for Fig. 2a,b, respectively. The higher indices in the case of Fig. 2b indicate the formation of a

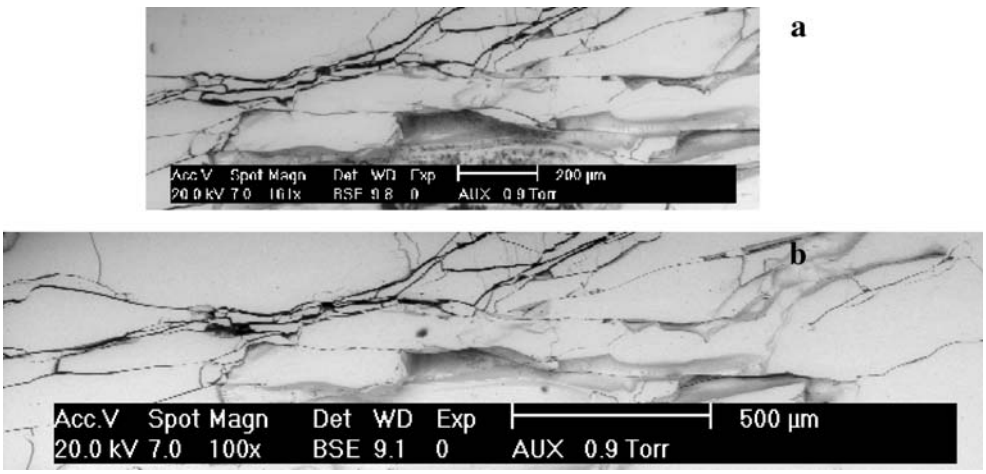

Fig. 4 Microphotograph of the $Zr_{0.43}Ni_{0.57}$ alloy before (**a**) and after (**b**) cycling in 0.1 M KOH

denser or higher protonated oxide than that in Fig. 2a. Microcrack sites at the surface may be more likely to be oxidised than other sites under similar electrochemical conditions [30]. For ZrO_2, the increase in k values is ascribed to a decrease in the O/Zr atomic ratio [18, 31], and also, higher k values are reported in the case of hydrogen insertion into the oxide [1, 12, 32]. Besides, in the case of steam-formed oxide, a significant higher value of extinction coefficient k than that of the anodically grown oxide has been reported [32–34]. Likewise, similar effects on the k index have also been observed in titanium oxide layers [12].

Figure 2c fits an $n-\mathrm{i}\,k$ equal to $1.42-\mathrm{i}\,0.55$ and a total d thickness variation of 18 nm. In this case, the lower values of n probably indicate the formation of a more hydrated or porous oxide layer on the Zn_2 alloy than on Zn_1.

Figure 2d fits $n-\mathrm{i}\,k$ values equal to $2.6-\mathrm{i}\,0.18$ and a total d change of about 2 nm for the B_6 alloy oxide layer. However, in this case, a higher dispersion in Ψ values is observed during cycling, and the process seems to be more complex with a potential dependence and hysteresis in the Δ/Ψ slope. This indicates a change in optical indices together with the progressive oxide film thickening, pointing to additional formation and removal of Cr hydride composites as well as Cr (II)/Cr(III) transformation [35–37].

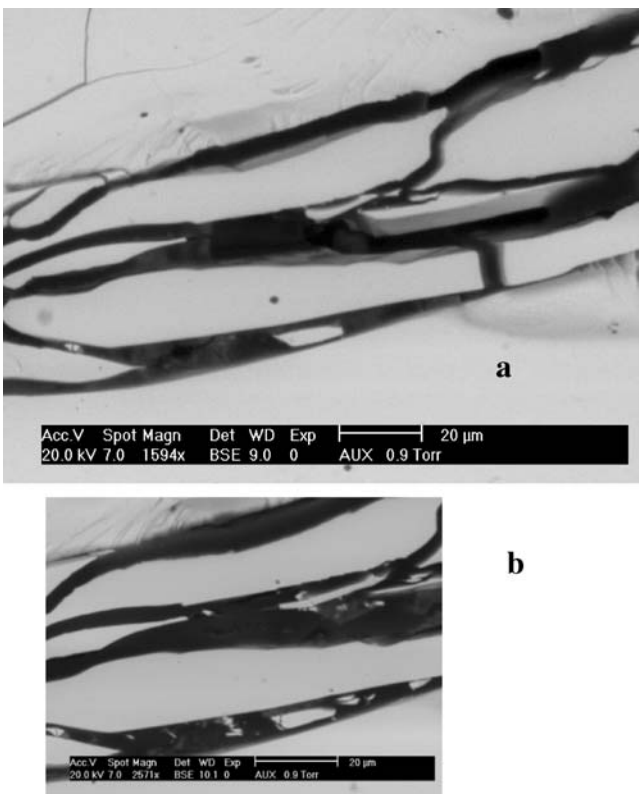

Fig. 5 Idem Fig. 4 but increasing 10×

Microscopic observation

Different sets of micrographs of the samples from the mechanically polished alloys, Zn_1, Zn_2 and B_6, were taken before and after applying an activation programme consisting of ten cycles between −0.4 and 0.3 V at a scanning potential rate of 0.5 mV/s. After activation and before the second micrograph, the samples were lightly polished using alumina 0.05 µm for 4 min to increase the contrast of crevices and grain boundaries. The different sets of SEM micrographs shown in Figs. 3, 4, 5, 6 and 7 allow us to

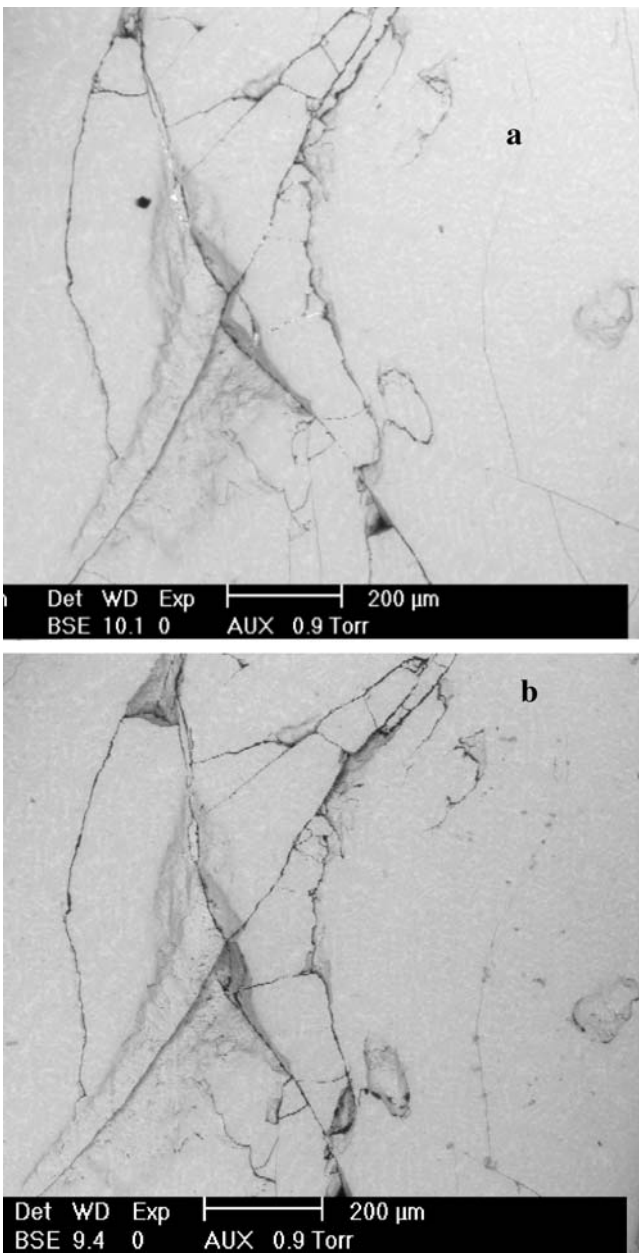

Fig. 6 Microphotograph of the $Zr_{0.9}Ti_{0.1}NiCr$ alloy before (**a**) and after (**b**) cycling in 0.1 M KOH

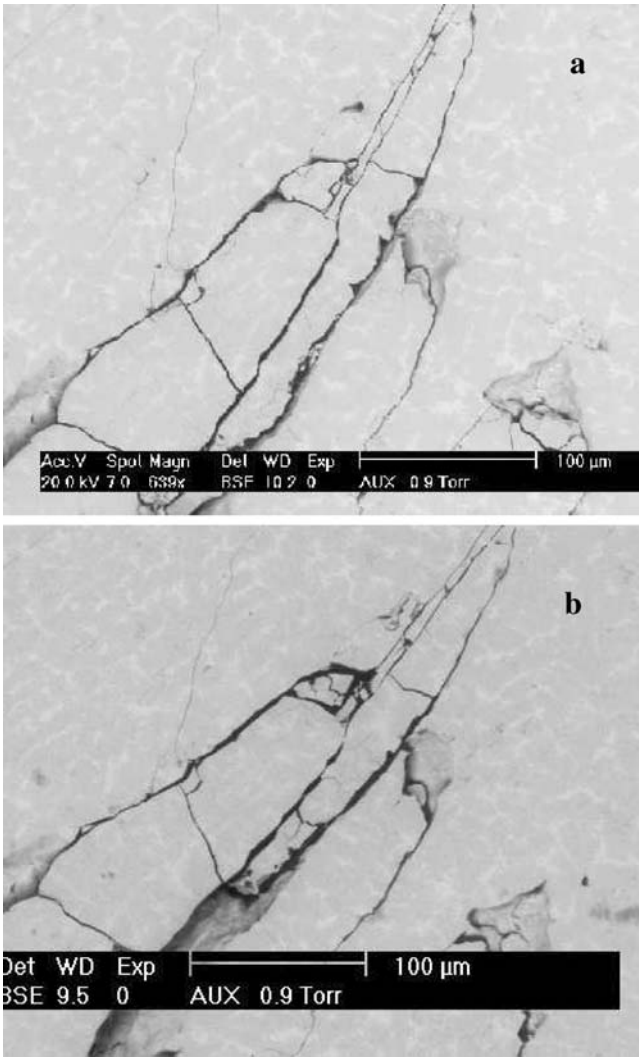

Fig. 7 Idem Fig. 6 increasing 3×

compare the surface effects before and after activation employing equivalent magnifications.

Figure 3 corresponding to Zn_1 shows a significant increase in the number and thickness of the crevices. Moreover, some grain detachment is also observed in areas surrounded by the highest cracks.

Figures 4 and 5 show the effect of activation for the Zn_2 alloys. Likewise, Figs. 6 and 7 correspond to B_6 alloy. In these cases, changes of about 1 and 5 μm in crevice size dimension are observed.

Table 1 EDAX results for the $Zr_{0.36}Ni_{0.64}$ alloy

Atom %	$Zr_{0.36}Ni_{0.64}$						
	On grain centre			Inside crevice after activation			
Ni	65.05	65.71	65.77	18.47	46.86	23.50	25.26
Zr	34.95	34.29	34.23	9.21	23.34	16.60	16.10
O				60.42	27.18	49.34	36.88
Al				10.51	1.82	10.15	21.74
K				1.39	0.81		

Table 2 EDAX results for the $Zr_{0.43}Ni_{0.57}$ alloy

Atom %	$Zr_{0.43}Ni_{0.57}$			
	On grain centre		Inside crevice before and after activation	
Ni	61.16	61.08	29.32	42.35
Zr	38.84	38.92	21.60	29.74
O			24.12	21.88
Al			24.97	6.03

The mechanism of crack propagation in H_2 gas media was modelled considering precipitation and fracture of hydrides at the crack tip [38] and the bulk hydrogen concentration in chemical equilibrium with the hydrogen gas. In this case, the crack tip velocity and the hydride volume fraction can be calculated as a function of the hydrogen diffusion rate and material deformation and strain. Furthermore, in aqueous media, a much more complex mechanism results owing to other determining factors such as applied electrochemical potential, local hydrogen pressure and oxide layers growing with different grades of partial protonation [23, 39, 40]. A similar process is also observed in water cooler nuclear reactors where an additional operating parameter is the intensity of β and γ beams. The irradiation increases the corrosion rate particularly in the thin film region, where electronic conduction through the oxide is considered the rate-limiting process for oxide growth [41]. In zircaloys, a delayed hydride cracking due to hydride precipitation close to the cladding outer surface, which is the coolest one, was also observed [42, 43].

In the case of AB_2 alloy subjected to potential cycling, the concomitant effect of potential cycling and change in hydrogen pressure may promote both chemical and mechanical transformations, thus allowing oxygen to penetrate deeply and corrode the alloy. In the case of pressurised water reactors, the combined effect of hydrogen and oxide layer growth together with temperature oscillations may play a similar synergy [44].

Table 3 EDAX results for the $Zr_{0.9}Ti_{0.1}NiCr$ alloy

Atom %	$Zr_{0.9}Ti_{0.1}NiCr$			
	On grain centre		Inside crevice before and after activation	
Ti	3.65	3.69	2.71	2.34
Cr	41.01	38.08	25.50	24.16
Ni	29.36	31.79	25.26	26.98
Zr	25.96	26.44	24.60	21.05
O			18.85	20.97
Al			3.09	4.50

On the other hand, the comparison between Figs. 2 and 5 reveals a large difference between the surface changes and those inside crevices. After activation, there is an oxide thickness growth of about 20 nm on the grain terraces, while the measured changes in the crevice dimension are about 1 μm. The enhanced corrosion processes inside the crevices indicates growth and dissolution of oxide layers induced by localised alkalinisation [45]. Although ZrO_2 solubility in 1 M KOH is very small (about 1.1 ppb), a mechanism based on surface reactions involving ZrOH and $HZrO_3^-$ dissolution and leading to crack initiation has been proposed [41]. Moreover, even if pre-charged hydrogen does not have a significant effect on both the pitting potential and on the calculated cleavage stress, when crevices are present, hydrogen accelerates the initiation and the progress of the corrosion crevice [45–48]. The polarisation and local pH changes increase the corrosion rate of these alloys particularly in the thin film region where electronic conduction through the oxide is higher and rules the rate process for oxide growth and dissolution [11, 49–54].

EDAX analysis

The chemical composition of the alloys and the resulting thin films are analysed by EDAX. The beam size has a resolution of about 1 μm^3 in the material. The compositional analysis of Zn1 and Zn2 shows very homogeneous values for different grains (Tables 1 and 2). However, the EDAX results for the crevices show more dispersion in composition values depending on the crevice size and beam position. Furthermore, a significant oxygen content is detected inside crevices. The oxide analysis is partially masked by the oxygen ions corresponding to alumina grains trapped into the cracks during polishing. The EDAX analysis on alumina particles shows a maximal atomic ratio O/Al of 2.0, while in most cases, inside crevices, a higher O/Al ratio is observed, indicating the presence of oxide passive layers. Zirconium oxide films may be substoichiometric increasing the O/Zr atomic ratio for increasing oxygen partial pressure [31]. The oxide growth inside crevices may produce high tensile stress field around the crack and promotes crevices propagation. This effect is superimposed to the induced cleavage due to hydride film formation [31, 55–57]. On the other hand, a relative increase in the Ni ratio in the presence of K^+ ions is observed (Table 1), indicating probable higher zirconium oxide dissolution for higher local alkalinisation. In the crevices, the nickel content decreases in the absence of K^+ ion accumulation (Tables 1 and 2). In the case of alloy B_6, chrome accumulation into crevices is detected [58] (Table 3). The nickel accumulation seems to be interdependent on the amount of other alloy components.

Conclusions

Stress corrosion cracking and the formation and reduction in protonated oxide layers are observed during the zirconium alloy activation. The activation process by potential cycling increases the thickness and decreases the compactness of the passive oxide layer and also increases crevice propagation. The cathodic polarisation through protonation of the oxide layer decreases the barrier effect and promotes oxide formation even at cathodic or near rest potentials. The effect of local anodic and cathodic polarisation, in addition to local pH changes inside crevices, promotes alloy dissolution. A combining effect of oxide growth and oxide dissolution promoted by the local alkalinisation principally works near the thin oxide interfaces.

Acknowledgements This work was supported by the Consejo Nacional de Investigaciones Científicas y Técnicas of Argentina, the Comisión de Investigaciones Científicas of Pcia. Bs. As. and the Agencia Nacional de Promoción Científica y Tecnológica. The authors thank both Dr. H. A. Peretti for supplying alloy samples and Ing. A. Pinto, Segemar, for his collaboration in microscopy observations.

References

1. Zerbino JO, Visintin A, Triaca WE (2005) J Solid State Electrochem 9:254
2. Taizhong H, Zhu W, Xuebin Y, Junzhou C, Baojia X, Tiesheng H, Naixin X (2004) Intermetallics 12:91
3. Visintin A, Peretti HA, Tori CA, Triaca WE (2001) Int J Hydrogen Energy 26:683
4. Kohlmann H, Fauth F, Yvon K (1999) J Alloys Compd 285:204
5. Jenq SN, Yang HW, Wang YY, Wan CC (1997) Mater Chem Phys 48:10
6. Liu BH, Lee JY (1997) J Alloys Compd 255:43
7. Cho SW, Han CS, Park CN, Akiba E (1999) J Alloys Compd 289:244
8. Fujii H, Pourarain F, Sunha VK, Wallace WE (1981) J Phys Chem 85:3112
9. Gebert A, Ismail N, Wolff U, Uhlemann M, Eckert J, Schultz L (2002) Intermetallics 10:1207
10. Hine F, Yasuda M, Sato H (1975) Corrosion NACE 33:181
11. Wilde BE, Hodge FG (1969) Electrochim Acta 14:619
12. DePauli CP, Giordano MC, Zerbino JO (1983) Electrochim Acta 28:1781
13. Habazaki H, Uozumi M, Konno H, Shimizu K, Nagata S, Asami K, Matsumoto K, Takayama K, Oda Y, Skeledon P, Thompson GE (2003) Electrochim Acta 48:3257
14. Meisterjahn P, Hoppe HW, Schultze JW (1987) J Electroanal Chem 217:159
15. Leach JSL, Nehru AY (1965) Corros Sci 5:449
16. Yamanaka S, Nishizaki T, Uno M, Katsura M (1999) J Alloys Compd 293–295:38
17. Zander D, Leptien H, Koster U, Eliaz N, Eliezer D (1999) J Non-Cryst Solids 250–252:893
18. Patrito EM, Macagno VA (1994) J Electroanal Chem 371:59
19. ElMotaal SMA, Hilal NH, Badawy WA (1994) Electrochim Acta 39:2611

20. Oliveira NTC, Biaggio SR, Rocha-Filho RC, Bocchi N (2002) J Braz Chem Soc 13:463
21. Guillemot F, Porte MC, Labrugere C, Baquey C (2002) J Colloid Interface Sci 255:75
22. Bertolino G, Perez Ipiña J, Meyer G (2006) J Nuclear Mater 348:205
23. Farina SB, Duffo GS, Galvele JR (2003) Corros Sci 45:2497
24. Ivanova SV (2006) Int J Hydrogen Energy 31:295
25. Une K, Ishimoto S (2003) J Nuclear Mater 322:66
26. Oskarsson M, Ahlberg E, Sodervall U, Andersson U, Pettersson K (2001) J Nuclear Mater 289:315
27. Shibutani H, Higashijima T, Ezaki H, Morinaga M, Kikuchi K (1998) Electrochim Acta 21–22:3235
28. Di Quarto F, Piazza S, Sunseri S, Yang M, Cai SM (1966) Electrochim Acta 41(16):2511
29. MacCrackin FL, Passaglia E, Stromberg RR, Steinberg HL (1963) J Res Natl Bur Stand A Phys Chem 67A:363
30. Nan JM, Tang Y, You JK, Li XQ, Lin ZG (1999) J Alloys Compd 293–295:747
31. Ben Amor S, Rogier B, Baud G, Jacquet M, Nardin M (1998) Mater Sci Eng B57:28
32. Ord JL, DeSmet DJ (1995) J Electrochem Soc 142:879
33. Michaelis A, Schweinsberg M (1998) Thin Solid Films 313–314: 756
34. Schweinsberg M, Michaelis A, Schultze JW (1997) Electrochim Acta 20–22:3303
35. Gerretsen JH, de Wit JHW (1990) Corros Sci 30:1075
36. Hones P, Diserens M, Levy F (1999) Surf Coat Technol 120–121 277
37. Paik W, Szklarska-Smialowska Z (1980) Surf Sci 96:401
38. Feng JL, Varias AG, Sui YK (2006) Int J Solids Struct 43:2174
39. Gutman EM (2004) Corros Sci 46:1801
40. Lim BH, Hong HS, Lee KS (2003) J Nuclear Mater 312:134
41. Cox B (2005) J Nuclear Mater 336:331
42. Root JH, Small WM, Khatamian D, Woo OT (2003) Acta Mater 51: 2041
43. Galvele JR (2003) Corros Sci 45:2119
44. Lelievre G, Fruchart D, Convert P, Lefevre-Joud F (2002) J Alloys Compd 347:288
45. Zeng YM, Luo JL, Norton PR (2004) Electrochim Acta 49:703
46. Domain C, Besson R, Legris A (2004) Acta Mater 52:1495
47. Suh D, Dauskardt RH (2002) Ann Chim Sci Mater 27:25
48. Murakami Y, Matsunaga H (2006) Int J Fatigue 28:1509
49. Amelinckx L, Kamrunnahar M, Chou P, Macdonald DD (2006) Corros Sci on line
50. Roustila A, Chene J, Severac C (2003) J Alloys Compd 356–357: 330
51. Szafranski AW (2002) J Alloys Compd 340:54
52. Kreeuer KD (1996) Chem Mater 8:610
53. Petot-Ervas G, Petot C (1990) J Phys Chem Solids 51:901
54. Pourbaix M (1966) Atlas of electrochemical equilibria. Pergamon, Cebelcor, Brussels
55. Sadoc A, Majzoub EH, Huett VT, Kelton KF (2003) J Alloys Compd 356–357:96
56. Liu YZ, Zu XT, Li C, Qiu SY, Li WJ, Huang XQ (2005) Scripta Materialia 52:821
57. Benzaid A, Huet F, Jerome M, Wenger F, Gabrielli C, Galland J (2002) Electrochim Acta 47:4333
58. Kolotyrkin YM (1980) Electrochim Acta 25:89